



# Acidic surface niobium pentoxide is catalytic active for CO<sub>2</sub> photoreduction

Gelson T.S.T. da Silva<sup>a,b</sup>, André E. Nogueira<sup>c</sup>, Jéssica A. Oliveira<sup>b,d</sup>, Juliana A. Torres<sup>b</sup>,  
Osmando F. Lopes<sup>e</sup>, Caue Ribeiro<sup>b,\*</sup>

<sup>a</sup> Department of Chemistry, Federal University of São Carlos (UFSCar), 13565-905, São Carlos, SP, Brazil

<sup>b</sup> National Nanotechnology Laboratory for Agribusiness (LNNa), Embrapa instrumentation, 13561-206, São Carlos, SP, Brazil

<sup>c</sup> Brazilian Nanotechnology National Laboratory (LNNano), CNPEM, 13083-970, Campinas, SP, Brazil

<sup>d</sup> Department of Chemical Engineering, Federal University of São Carlos (UFSCar), 13565-905, São Carlos, SP, Brazil

<sup>e</sup> Federal University of Uberlândia, Institute of Chemistry, Santa Mônica, 38400-902, Uberlândia, MG, Brazil

## ARTICLE INFO

### Keywords:

CO<sub>2</sub> reduction mechanism

Surface acidity

Nb<sub>2</sub>O<sub>5</sub>

Artificial photosynthesis

## ABSTRACT

In this paper, we report for the first time the significant photocatalytic activity of Nb-based materials for CO<sub>2</sub> reduction. Nb<sub>2</sub>O<sub>5</sub> catalysts were prepared through a modified peroxide sol-gel method using different annealing temperatures, showing activity for CO<sub>2</sub> photoreduction in all conditions. The activity and selectivity of the Nb<sub>2</sub>O<sub>5</sub> samples were directly related to their surface acidity: high surface acidity prompted conversion of CO<sub>2</sub> to CO, HCOOH, and CH<sub>3</sub>COOH; low surface acidity prompted conversion of CO<sub>2</sub> to CH<sub>4</sub>. The results also indicated that CO is the main intermediate species of the CO<sub>2</sub> photoreduction in all conditions. We have uncovered the role played by the surface acidity of Nb<sub>2</sub>O<sub>5</sub> and the mechanism behind its performance for CO<sub>2</sub> photoreduction.

## 1. Introduction

Since atmospheric carbon dioxide (CO<sub>2</sub>) concentration has been increasing, leading to greenhouse effects [1–3], the development of photocatalysts to prompt CO<sub>2</sub> reduction is promising for both environmental (reducing total CO<sub>2</sub> emission) and economic management. CO<sub>2</sub> reduction yields fuels or sustainable chemicals (CH<sub>4</sub>, CO, CH<sub>3</sub>OH, etc.) that are suitable for power generation or industrial processes [4,5]. However, there is a challenge that lies in an adequate photocatalyst development: improvements in the CO<sub>2</sub> photoconversion rates and the study on the mechanisms involved in this process are required [6,7]. The photoconversion efficiency and selectivity of catalysts towards desired products depend on their light absorption and charge separation efficiencies and spatial position of valence and conduction bands, however the catalyst surface properties also play a critical role in the charge transference process [8,9].

The literature reports several CO<sub>2</sub> photoreduction approaches that use water simultaneously as a dissolution medium and electron source [10–12]. Typical setups involve the bubbling of CO<sub>2</sub> into alkaline medium to prompt high reactant concentrations [7,13], as well as the investigation of the basic-surface catalyst effects on CO<sub>2</sub> adsorption [14,15]. Some authors indicate that due to the CO<sub>2</sub> acidic character, basic catalysts are more likely for adsorption and further to react with CO<sub>2</sub> by electron transference. However, we propose here that acidic

catalysts, due to their role as an electron acceptor, can be active for CO<sub>2</sub> reduction as well as for specific molecular bonding, which depends on their adequate charge separation when excited by light [16–18]. To the best of our knowledge, Nb<sub>2</sub>O<sub>5</sub> is a semiconductor that fulfills both features: it shows good performance as a catalyst due to its very acidic surface [19–22] and exhibits photoactivity for pollutant degradation [23–26]. Nevertheless, studies on the photocatalytic activity of Nb<sub>2</sub>O<sub>5</sub> for CO<sub>2</sub> reduction have not been published yet.

We describe here that Nb<sub>2</sub>O<sub>5</sub> can be a very active catalyst for CO<sub>2</sub> photoreduction with formation of preferential byproducts driven by the Nb<sub>2</sub>O<sub>5</sub> surface acidity. A series of Nb<sub>2</sub>O<sub>5</sub> catalysts were synthesized through a modified peroxide sol-gel method. Our results support a deep discussion about the role of the surface acidity of photocatalytic semiconductors, providing important insights into the design of selective CO<sub>2</sub> reduction systems.

## 2. Experimental

### 2.1. Synthesis

The precursor ammonium niobium oxalate (CBMM, Brazil) was dissolved in distilled water (140 mL) under vigorous stirring and then 60 mL of hydrogen peroxide was added to the solution, leading instantaneously to a transparent yellow solution, which denotes

\* Corresponding author.

E-mail address: [caue.ribeiro@embrapa.br](mailto:caue.ribeiro@embrapa.br) (C. Ribeiro).

<https://doi.org/10.1016/j.apcatb.2018.10.017>

Received 30 July 2018; Received in revised form 5 October 2018; Accepted 7 October 2018

Available online 09 October 2018

0926-3373/ © 2018 Elsevier B.V. All rights reserved.

formation of niobium peroxo complex. Afterward, the niobium peroxo complex solution was heated at 80 °C for 1 h and a yellow gel was formed. The product was allowed to cool down to room temperature, recovered by centrifugation, and dried in air at 60 °C for 12 h. The final product is reactive niobium pentoxide with surface modified with peroxo groups (namely Nb-OPM) [23,27]. This Nb-OPM was annealed at 150, 200, 300, 400 and 600 °C for 2 h using heating rate of 10 °C min<sup>-1</sup> in alumina crucible boats. Samples were referred to as Nb-x, where x represents the annealing temperature.

## 2.2. Characterizations

The crystalline phases were characterized by X-ray diffraction (XRD) over the 2θ range from 10 to 80° using a Shimadzu XRD-6000 diffractometer operating with CuKα radiation. Thermal analyses were carried out using a TGA Q500 thermogravimetric analyzer (TA Instruments) in air atmosphere from room temperature up to 700 °C using heating rate of 10 °C min<sup>-1</sup>. A Fourier Transform Infrared spectrometer (FTIR) (Bruker VERTEX 70) was used to investigate surface changes using sample-containing KBr disks with 64 scans and 4 cm<sup>-1</sup> resolution in the 4000–400 cm<sup>-1</sup>. Raman spectroscopy was performed with a FT-Raman spectrometer (Bruker RAM II with a Ge detector), equipped with a Nd:YAG laser with wavelength centered at 1064 nm generating a power of 150 mW at a resolution of 4 cm<sup>-1</sup>. Sample morphology and particles size were analyzed by field emission gun scanning electron microscopy (FEGSEM) JEOL JSM 6701 F. The materials were also characterized by transmission electron microscopy (TEM), using an FEI Tecnai G2 F20 microscope. N<sub>2</sub> adsorption-desorption isotherms were measured with a Micromeritics ASAP 2020 analyzer at 77 K. Samples were previously degassed at 80 °C under vacuum until a degassing pressure < 10 μmHg. The Brunauer–Emmett–Teller (BET) method was used to calculate the specific surface area (S<sub>BET</sub>). The total pore volume (V<sub>p</sub>) was estimated from the adsorbed N<sub>2</sub> amount at a relative pressure P/P<sub>0</sub> of 0.98. UV–vis diffuse reflectance spectroscopy (DRS) was measured at room temperature from 200 to 800 nm in a Varian Cary 5 G spectrophotometer in diffuse reflectance mode (R). CHN analyses were conducted on a Perkin Elmer 2400 elemental analyzer.

The total amount of acid sites in the Nb<sub>2</sub>O<sub>5</sub> samples was measured by the ionic-exchange procedure followed by titration of the acid species released from the solid acid in alkaline solution using a calibrated pH meter (QX 1500 Plus Qualxtron) [28,29]. First, 0.1 g of samples were placed in a vial containing 10 mL of 0.1 mol L<sup>-1</sup> NH<sub>4</sub>OH solution. The vial was sealed and kept under constant stirring for 12 h and the resulting suspension was titrated with 0.1 mol L<sup>-1</sup> HCl solution. The total acidity was calculated using the following equation [28,29]:

$$C_{as} = \frac{[(C_{NH_4OH})(V_{NH_4OH})] - [(C_{HCl})(V_{HCl})]}{m_{cat}} \quad (1)$$

where C<sub>as</sub> is the acid sites concentration, C<sub>NH<sub>4</sub>OH</sub> is the NH<sub>4</sub>OH concentration (mol L<sup>-1</sup>), C<sub>HCl</sub> is the HCl concentration (mol L<sup>-1</sup>), V<sub>NH<sub>4</sub>OH</sub> represents the NH<sub>4</sub>OH solution volume, V<sub>HCl</sub> is the HCl solution volume and m<sub>cat</sub> is the sample amount (g).

## 2.3. CO<sub>2</sub> photoreduction

The CO<sub>2</sub> photoreduction was performed in a cylindrical steel reactor covered with borosilicate glass with 225 mL total volume. In brief, 0.1 g of catalyst were suspended in 100 mL of distilled water. High purity CO<sub>2</sub> was bubbled into the reactor for 20 min to expel the remaining gases and saturate the water inside the reactor. The reactor was then uniformly illuminated from the inside using a UVC lamp (PHILIPS 5 W) protected by a quartz tube with a maximum wavelength of 254 nm (0.167 mW/cm<sup>2</sup>) (Fig. S1). The photocatalytic performance of the Nb<sub>2</sub>O<sub>5</sub> samples was monitored every 60 min for 6 h by collecting 0.3 mL of the gaseous sample with a watertight syringe, which was injected

into a gas chromatograph (GC) to analyze the amount of CO and CH<sub>4</sub> formed inside the reactor. The experiments were also conducted in the absence of catalyst and light and no appreciable amounts of products could be detected, indicating that both are required for the photocatalytic CO<sub>2</sub> reduction. To determine the amount of CO<sub>2</sub> converted into hydrocarbons or carbon monoxide, the equation described below was used, taking into account the concentration of the products formed and the concentration of CO<sub>2</sub> in water, assuming that the solution is saturated with CO<sub>2</sub>.

$$\text{Amount of CO}_2 \text{ Converted [\%]} = \frac{\text{Product concentration}}{\text{CO}_2 \text{ concentration}} \times 100 \quad (2)$$

Gaseous products were determined by gas chromatography (GC, Varian, CP-3800) equipped with a thermal conductivity detector (TCD) and a flame ionization detector (FID), using a packed column (HayeSep N (0.5 m x 1.8")) with flow rate of 30 mL min<sup>-1</sup> for H<sub>2</sub>, 300 mL min<sup>-1</sup> for air and 30 mL min<sup>-1</sup> for N<sub>2</sub>. The injector temperature was set at 150 °C, while the TCD and FID detector temperatures were 200 °C and 150 °C, respectively. The gas products were analyzed by the external standard method.

High-performance liquid chromatography (HPLC-LC-20AD, Shimadzu) was used to analyze the products formed in the liquid phase. Samples (20 μL) were collected after 6 h of CO<sub>2</sub> photoreduction and injected into an Aminex HPX-87H column (300 x 7.8 mm), which is suitable for carboxylic acid and alcohol determination, using dilute H<sub>2</sub>SO<sub>4</sub> solution (0.33 mmol L<sup>-1</sup>) as a mobile phase flowing at 0.6 mL min<sup>-1</sup>. Column and detectors were kept at constant temperature of 40 °C. This chromatograph was equipped with a differential refractive index detector (RID-10 A) suitable for alcohols quantification and a UV–vis detector (SPD-20 A, 210 nm) with deuterium lamp suitable for carboxylic acid determination.

## 3. Results and discussion

### 3.1. Characterization of Nb<sub>2</sub>O<sub>5</sub> samples

XRD patterns of Nb ammonium oxalate and Nb<sub>2</sub>O<sub>5</sub> samples are shown in Figs. 1 and S3. It is observed that the Nb ammonium oxalate precursor is crystalline, but it becomes amorphous (up to 480 °C) when treated with hydrogen peroxide to form Nb-OPM. This indicates the proper reaction, forming a hydrated niobium pentoxide (Nb<sub>2</sub>O<sub>5</sub>·nH<sub>2</sub>O), also known as niobic acid [19,20,30,31]. The calcination at different temperatures indicates that the hydrated niobium pentoxide is stable even at high temperatures, i.e. hydration corresponds to strongly

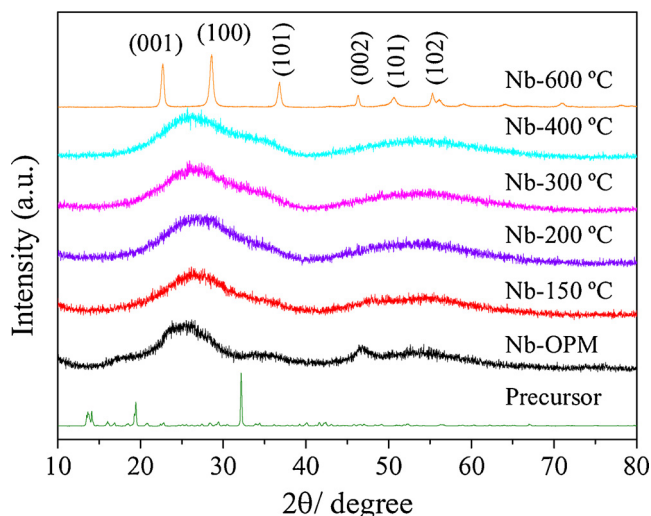


Fig. 1. XRD patterns for Nb precursor and Nb<sub>2</sub>O<sub>5</sub> samples obtained by oxidant peroxide method (OPM) and after calcination from 150 to 600 °C.

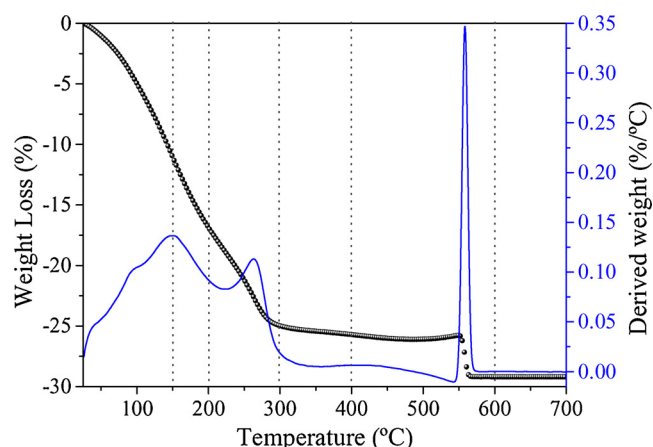


Fig. 2. Thermogravimetric Analysis of Nb-OPM. Dotted lines indicate the temperatures related to the calcined samples.

bonded water instead of water weakly adsorbed at the niobium pentoxide structure [29]. In fact, as seen in Fig. 2, TGA/DTG curves show that Nb-OPM loses around 5% weight up to 100 °C, associated with physically/weakly adsorbed water molecules. The most significant weight loss (~20%) lies in the temperature range between 100 and 300 °C, which is associated with residual organic molecules (CO and OCO) of the precursor and strongly adsorbed surface water or with the crystalline oxide network [32]. Above 500 °C, there are weight losses associated with the complete oxide dehydration, which results in a crystalline material (Fig. S3). This agrees with the XRD pattern of Nb-600 °C, which shows the formation of the pseudo-hexagonal phase of Nb<sub>2</sub>O<sub>5</sub> with high crystallinity (JCPDS No. 07-061) [32,33]. Therefore, these results indicate that samples are structurally similar from room temperature until 480 °C due to the presence of adsorbed and structural water molecules.

The surface water molecules are also perceived by FTIR, as seen in Fig. 3. The broad vibration band in the range 3471 cm<sup>-1</sup>–3126 cm<sup>-1</sup> relates to the OH-stretching vibration of H<sub>2</sub>O molecules and structural OH-groups – this band is observed in the FTIR spectra of all samples except Nb-600 °C [34]. However, its intensity decreases with the increasing of calcination temperature, thus agreeing with the TGA results. The FTIR spectrum of Nb-400 °C exhibits minimal band intensity, indicating that weakly absorbed water content is also low – although this sample corresponds to a hydrated Nb<sub>2</sub>O<sub>5</sub> material, as indicated by XRD. The FTIR spectrum of Nb-600 °C presents a small shift in this band regarded to Nb-OH stretching, which agrees with the role of structural water in the thermal phase transition of Nb<sub>2</sub>O<sub>5</sub> [23,29]. Comparing the

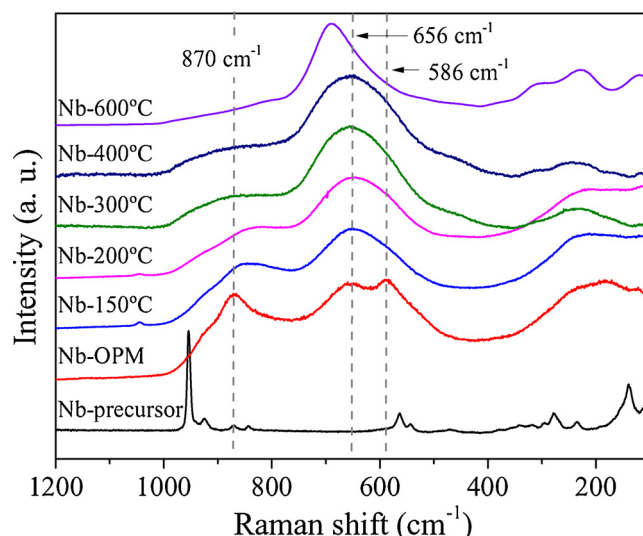


Fig. 4. Raman spectra for Nb-samples set: Nb-OPM, Nb-150 °C, Nb-200 °C, Nb-300 °C, Nb-400 °C, and Nb-600 °C.

XRD patterns, it is seen that these amounts are not effective to keep the hydrated Nb<sub>2</sub>O<sub>5</sub> phase unchanged, which may influence its final properties. Vibration bands at the range 1840–1305 cm<sup>-1</sup> correspond to organic byproducts from reactants, which are almost totally eliminated at 400 °C [35]. Characteristic peaks attributed to Nb–O groups of niobium oxide are observed below 1144 cm<sup>-1</sup> in all FTIR spectra [34,35].

The strong scattering properties of the Raman spectra can be further used to analyze the phase structure features in the catalysts. Fig. 4 exhibits the Raman spectra of the precursor and Nb-x samples. The Raman spectrum of the Nb precursor exhibits narrow and very intense peaks, which is characteristic of materials with good crystallinity, which agrees with the XRD results. The Raman spectrum of Nb-OPM shows three representative signals, one centered at 870 cm<sup>-1</sup> and two centered at 656 and 586 cm<sup>-1</sup>. The peak centered at 870 cm<sup>-1</sup> and the peak centered at 586 cm<sup>-1</sup> can be attributed to the symmetrical and asymmetric stretching of NbO<sub>2</sub> groups and associated with formation of di-η<sup>2</sup>-peroxo systems with *cis*-lateral geometry. The signal centered at 656 cm<sup>-1</sup> can be attributed to the asymmetric stretching of Nb–O groups in the distorted polyhedra of NbO<sub>6</sub>, NbO<sub>7</sub> and NbO<sub>8</sub>, thus characterizing the amorphous state of the materials. It is important to note that intensity of the peaks at 870 and 586 cm<sup>-1</sup> signals decrease since the first thermal treatment (200 °C), indicating the gradual loss of peroxide groups (O–O and O–H). For 600 °C (Nb-600 °C), the peak

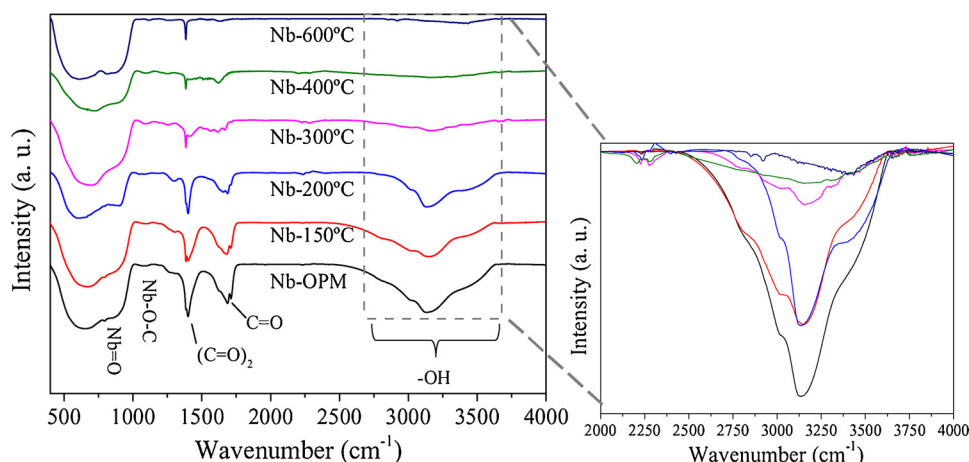
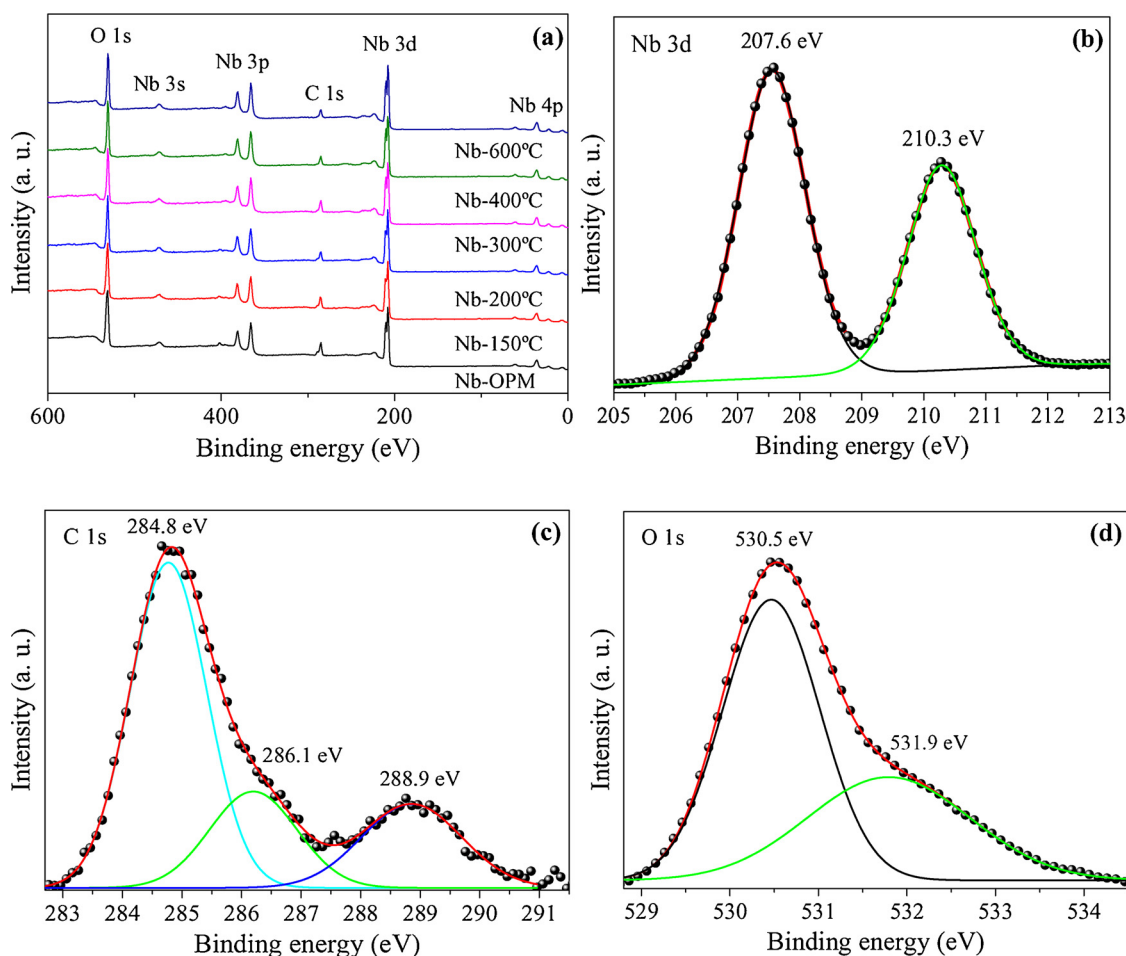


Fig. 3. Full and enlarged FTIR spectra of Nb-samples obtained without heating (Nb-OPM) and at 150, 200, 300, 400 and 600 °C.



**Fig. 5.** (a) XPS survey spectra of synthesized samples and high-resolution XPS spectra with deconvolution curves for (b) Nb 3d, (c) C 1s and (d) O 1s of the Nb-OPM sample.

centered at  $656\text{ cm}^{-1}$  shifts to  $692\text{ cm}^{-1}$  and becomes more defined, indicating the formation of pseudohexagonal phase [35–37].

Full-scale XPS spectra (Fig. 5a) indicate the presence of Nb, C, and O at the surface of the Nb-x samples. The Nb 3d high-resolution XPS spectra show Nb 3d peaks at 207.6 eV and 210.3 eV, corresponding to Nb  $3d_{3/2}$  and Nb  $3d_{5/2}$  levels, respectively, indicating Nb<sup>5+</sup> oxidation state and niobium pentoxide formation (Nb<sub>2</sub>O<sub>5</sub>) in all conditions (Figs. 5b and S3e) [32,38]. In the C 1s and O 1s high-resolution XPS spectra (Fig. 5c,d), the contribution of carboxyl and hydroxyl groups is noticeable, mainly for the Nb-OPM sample. The C 1s XPS spectra are shown in Fig. 5c, giving three different C signals (the strongest peak at 284.8 eV is assigned to the adventitious hydrocarbon from the XPS instrument). The other two weak peaks at 286.1 eV and 288.9 eV are identified as carbon oxygen bond species (CO, OCO), probably residual contaminants of the oxalate precursor [33,39]. The O 1s region after the deconvolution curves can be seen in Fig. 5d, showing two peaks characteristics of Nb–O bond (530.5 eV) as well as oxygen in hydroxyl groups (531.9 eV), assigned to water molecules adsorbed at the Nb-x sample surfaces [39,40]. In both cases (C 1s and O 1s), the increase in the annealing temperature decreases the intensity of the peak attributed to carboxyl and hydroxyl groups, as observed in Fig. S3a–d. This corroborates with the TGA results, that is, the increase in temperature leads to loss of weakly adsorbed water molecules, followed by loss of strongly adsorbed water molecules with carboxyl groups and finally the total crystallization of the Nb-x samples, as confirmed by XRD.

Bandgap values obtained by interpolation of diffuse reflectance spectroscopy curves (Fig. S4) show that the energies required to excite each photocatalyst are quite similar (Table 1), except for Nb-OPM,

**Table 1**

The surface areas, pore volumes and electronic properties of Nb<sub>2</sub>O<sub>5</sub>-OPM calcined at different temperature.

Sample	S <sub>BET</sub> (m <sup>2</sup> /g) <sup>a</sup>	V <sub>p</sub> (cm <sup>3</sup> /g) <sup>b</sup>	Bandgap (eV)
Nb-OPM	18	0.012	2.6
Nb-150 °C	13	0.013	3.0
Nb-200 °C	11	0.012	3.0
Nb-300 °C	11	0.013	3.2
Nb-400 °C	10	0.013	3.2
Nb-600 °C	20	0.037	3.1

<sup>a</sup> Surface area obtained by BET method.

<sup>b</sup> Total pore volume.

which is influenced by remnant peroxocomplex structure. Therefore, from 150 °C to 600 °C, the differences are minimal, denoting the similar electronic property among the Nb-x samples.

The morphology and size of the Nb<sub>2</sub>O<sub>5</sub> particles were examined by scanning electron microscopy (SEM) and transmission electron microscopy (TEM). As shown in Figs. 6 and S5, all samples are micrometric agglomerates of nanoparticles. The Nb-600 °C sample is composed of denser nanometric agglomerates than Nb-OPM and Nb-400 °C samples, thus indicating growth of Nb<sub>2</sub>O<sub>5</sub> nanoparticles at high temperatures (recrystallization and coalescence process). Table 1 shows that the specific surface area values decrease with the increasing calcination temperature (up to 400 °C), which may be related to the decrease of sample surface roughness caused by the growth of the particles. However, the Nb-600 °C sample exhibits an increase in the specific surface



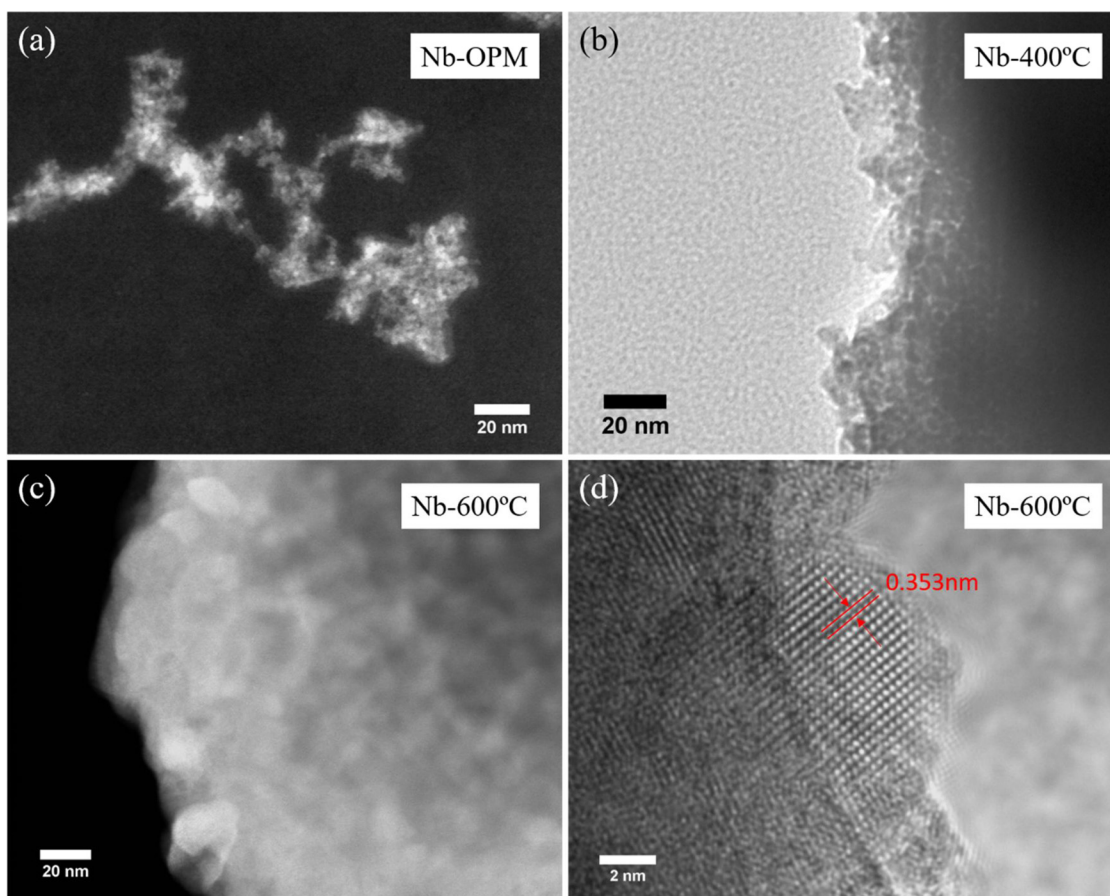


**Fig. 6.** Transmission electron microscopy (TEM) images of (a) Nb-samples obtained without heating (Nb-OPM) and annealed at (b) 400 and (c) 600 °C. (d) High-magnification transmission electron microscopy (HRTEM) image of Nb-600 °C sample.

area, indicating that the nucleation-recrystallization processes induced the formation of a phase with lower density. The total pore volume values of the samples calcined up to 400 °C are similar (Table 1), however, they are lower than that of the Nb-600 °C sample, indicating that water molecules or precursor residues are totally eliminated at 600 °C (Table S1), leaving the pores free, and consequently, increasing the pore volume and surface area.

### 3.2. Photocatalytic performance of Nb<sub>2</sub>O<sub>5</sub> samples

Fig. 7 shows the photocatalytic performance of the Nb-*x* samples for CO<sub>2</sub> reduction to CO and CH<sub>4</sub> in aqueous medium. It is observed a preference for CO formation after 6 h of reaction under UV irradiation. However, the CO production efficiency decreases with the increasing of the annealing temperature.

The Nb-OPM sample shows the highest performance towards CO production (over 10.7 mmol L<sup>-1</sup> g<sup>-1</sup>), compared to the other samples, as can be seen in Fig. 7a. This behavior may be associated with the photoreduction of organic groups (oxalate) present at the catalyst surface and not with the direct reduction of CO<sub>2</sub> molecules, since the vibrations attributed to the oxalate groups decrease after the reaction (according to Fig. S7) [23,35]. To confirm this hypothesis, the stability of Nb-OPM was evaluated over five 6-h photocatalysis cycles, (Fig. 8a). It is observed that the CO production decreases abruptly up to the third cycle, leveling off in the fourth and fifth cycles. This demonstrates that part of the CO produced over the photocatalysis relates to the organic groups at the catalyst surface. However, even after the fifth photocatalysis cycle the Nb-OPM sample still prompts CO production rate (257 μmol L<sup>-1</sup> g<sup>-1</sup>) [41–43].

An important aspect is the CO production yield stabilization after 4-

h of photocatalysis (Fig. 7a) for Nb-OPM. This should be interpreted by the availability of CO<sub>2</sub> for reduction *versus* CO solubility in water. As the CO<sub>2</sub> solubility (1.45 g L<sup>-1</sup>) in aqueous medium is higher than the CO solubility (0.027 g L<sup>-1</sup>), higher CO<sub>2</sub> amount is available to react with the catalysts [44,45]. Therefore, CO is formed and easily saturates the medium, most of the CO molecules diffuse to the photoreactor headspace, demonstrating the tendency for a plateau after 4 h. Amount of CO<sub>2</sub> converted data are depicted in Table 2, considering that each 1 mol of CO or CH<sub>4</sub> is produced at the expense of 1 mol of CO<sub>2</sub> [46,47].

Regarding the CH<sub>4</sub> production, Nb-OPM initially presents photocatalytic activity similar to the other samples, except for Nb-400 °C which prompts a CH<sub>4</sub> production of 4.78 μmol.L<sup>-1</sup>.g<sup>-1</sup>. This may be associated with the residual organic molecules, decreasing CO<sub>2</sub> interaction in aqueous medium and blocking the catalytic sites. This is confirmed by the presence of oxalate peaks (1840 – 1305 cm<sup>-1</sup>), which are reduced after the CO<sub>2</sub> photoreaction with Nb-OPM, indicating the presence of related organic groups. However, as observed in Fig. 8, from the second cycle onwards there is an increase in the CH<sub>4</sub> production, confirming that these organic molecules block the interaction of CO with the catalyst surface. On other hand, after the removal of organic residues the CO can be adsorbed on the Nb<sub>2</sub>O<sub>5</sub> surface, and the CO can be converted to CH<sub>4</sub>. This pathway is thermodynamically and kinetically more favorable than the reduction of CO<sub>2</sub> towards CH<sub>4</sub> [12,48–50]. Inversely to the plateau for CO production (Fig. 7a), the CH<sub>4</sub> production tends to increase gradually, especially for Nb-400 °C (Fig. 7b). This suggests that the CH<sub>4</sub> production relates to the CO excess in solution, leading to a basic mechanism for CH<sub>4</sub> production in which CO is the intermediary species in the catalytic system [7,51]. Since Nb-400 °C has a few surface hydroxyl groups, this suggests that the CO to CH<sub>4</sub> conversion mechanism probably depends on the affinity of CO to

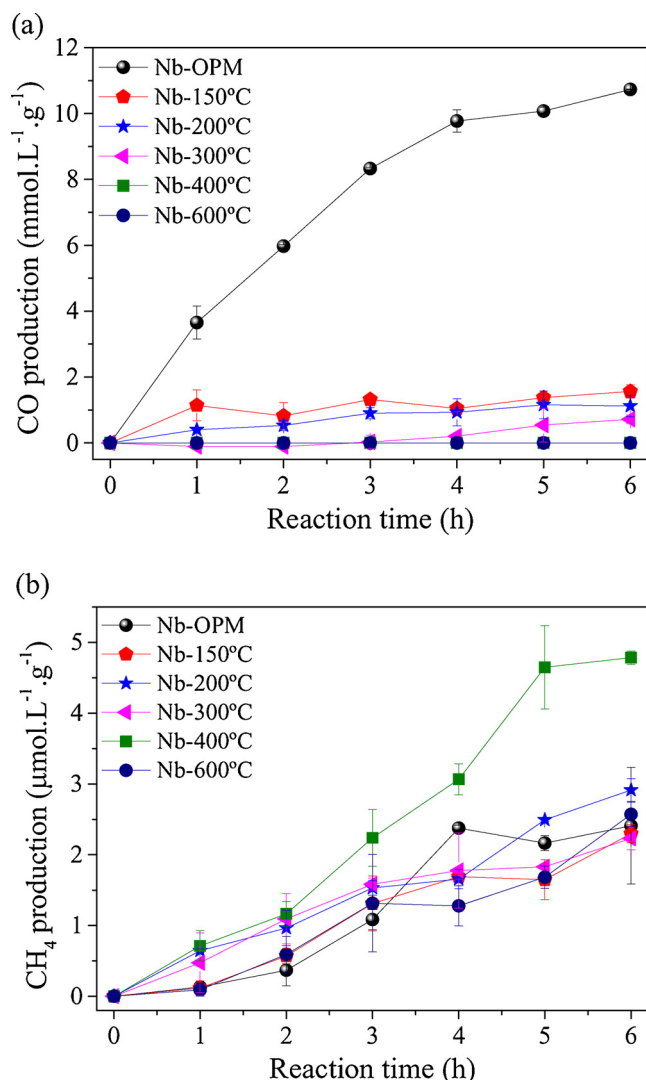


Fig. 7. Gaseous byproducts of CO<sub>2</sub> photoreduction according to the catalyst: (a) CO and (b) CH<sub>4</sub>.

the catalyst surface [4,48,52–55]. This is confirmed by the higher photocatalytic activity of Nb-400 °C for CH<sub>4</sub> production since this sample still exhibits the same crystalline structure at 400 °C (niobic acid, Nb<sub>2</sub>O<sub>5</sub>·nH<sub>2</sub>O) but with minor surface hydroxyls and organic adsorbates. Comparing to the Nb-600 °C sample, which is also free of these organic groups but shows poor catalytic activity, the results confirm that niobic acid is the catalytic active phase, and that the surface acidity plays an important role in the CO<sub>2</sub> photoreduction selectivity [30,56].

Similar to the gas phase, two products are observed in the liquid phase (Fig. 9), namely, formic acid (HCOOH) and acetic acid (CH<sub>3</sub>COOH), with a very similar tendency. The highest liquid-phase product yields are obtained with the most hydroxylated catalysts (Nb-OPM and Nb-150 °C), denoting the advantage of the coordinately unsaturated-surface samples. Surprisingly, the Nb-400 °C sample (which prompted CH<sub>4</sub> production at a highest extent) shows decreased activity for liquid-phase products formation, which highlights the role of the surface hydroxyl group amount in the catalyst selectivity. This role is probably related to the surface acidity (Table 2), suggesting that Nb-OPM is the most effective acid catalyst, followed by Nb-150 °C and Nb-200 °C. This decrease was effective to suppress the CO production at a very low level compared to Nb-OPM, but it is still remarkable that Nb-150 °C is active for HCOOH and CH<sub>3</sub>COOH production. The surface acidity tends to decrease as the annealing temperature increase, and the

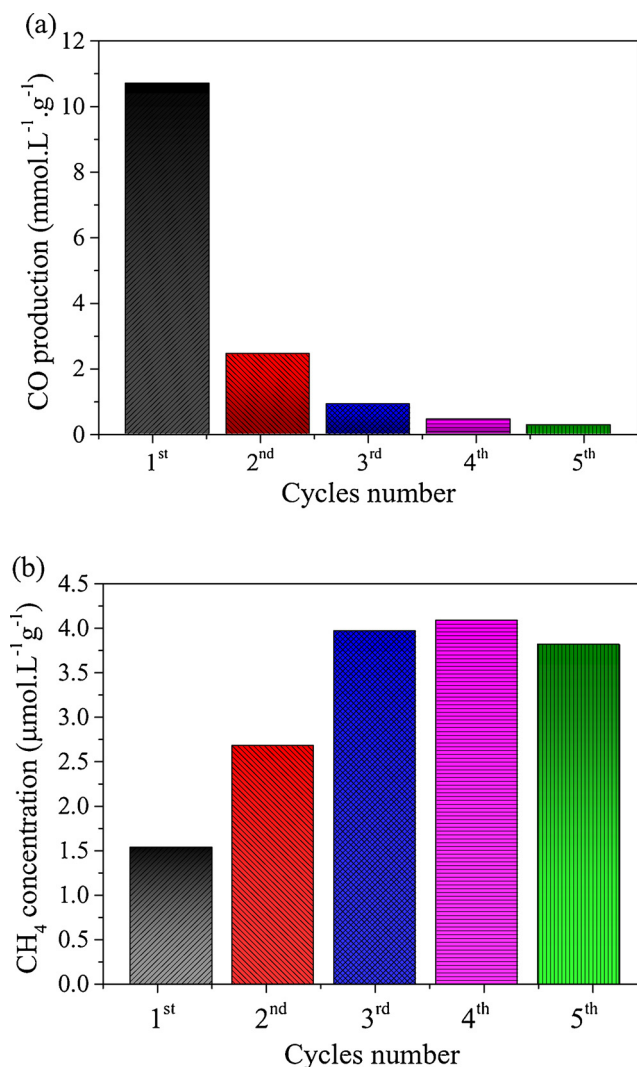


Fig. 8. Nb-OPM stability during 5 reusing cycles. (a) CO formation and (b) CH<sub>4</sub> production.

Table 2

Total acid site concentration (C<sub>as</sub>) of synthesized samples and amount of CO<sub>2</sub> converted after 6 h of reaction.

Samples	C <sub>as</sub> (mmol/g)	Amount of CO <sub>2</sub> Converted (%)			
		CO	CH <sub>4</sub>	CH <sub>3</sub> COOH	HCOOH
Nb-OPM	2.5	9.75	2.2	21.6	18.4
Nb-150 °C	1.4	1.42	2.1	34.3	43.7
Nb-200 °C	1.2	1.02	2.7	7.1	2.2
Nb-300 °C	0.8	0.65	2.0	2.2	5.9
Nb-400 °C	0.4	*	4.4	11.7	4.9
Nb-600 °C	0.0	*	2.3	7.3	1.1

activity towards HCOOH and CH<sub>3</sub>COOH formation as well.

It is noteworthy that the yields of formic and acetic acid were larger in all conditions than the CH<sub>4</sub> yields. With basis on this comparison, one could notice that the CH<sub>4</sub> production, in any condition, is very below the production of other compounds, reinforcing the hypothesis that the mechanism involves the successive reactions of CO with H<sup>+</sup>, leading to formic and acetic acid. It is impressive that the production of these intermediate species is remarkably high, thereby showing the versatility of Nb<sub>2</sub>O<sub>5</sub> as a catalyst for CO<sub>2</sub> photoreduction.

It is demonstrated that semiconductors, such as Nb<sub>2</sub>O<sub>5</sub>, having acidic surface can be used as photocatalysts for conversion of CO<sub>2</sub> to CO

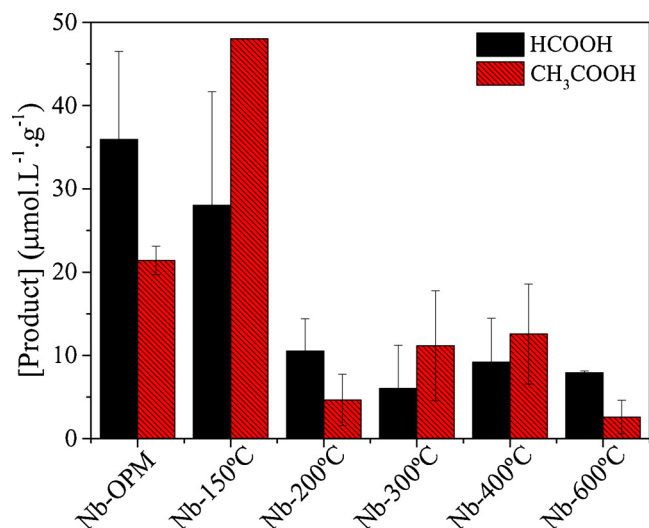


Fig. 9. Peak amounts of the main compounds obtained by photocatalytic reduction of CO<sub>2</sub> with H<sub>2</sub>O on synthesized Nb-samples, after 6 h.

or hydrocarbons. Thus, we propose a reaction mechanism (Scheme 1) based on several steps: in the 1<sup>st</sup> step, there is physisorption of the CO<sub>2</sub> molecules on the photocatalyst surface, which is comprised of a high number of hydroxyl groups. Afterwards (2<sup>nd</sup> step), the catalyst is activated by UV radiation, generating charge carriers, which induce reductive and oxidative processes. In the valence band, oxygen from water is oxidized to molecular oxygen (Fig. S8) while the excited electron are transfers to the CO<sub>2</sub> molecules, generating CO<sub>2</sub><sup>•-</sup> species [57,58]. The CO<sub>2</sub><sup>•-</sup> species are reduced through a series of complex and elementary steps involving the transfer of an electron, a proton or a hydrogen radical, as well as the breakage of C–O bonds and the creation of new C–H bonds [7,48,59]. Several of the intermediates are radical species whose recombination at different stages partially explains the number of possible pathways and end products.

Therefore, based on the results presented here, we propose that

carbon monoxide (CO) and formic acid (HCOOH) are the first species formed from the CO<sub>2</sub> photoreduction in gas and liquid phase, respectively. This is probably due to the fact that these reactions require only two electrons and two protons (3<sup>rd</sup> step) [59,60].

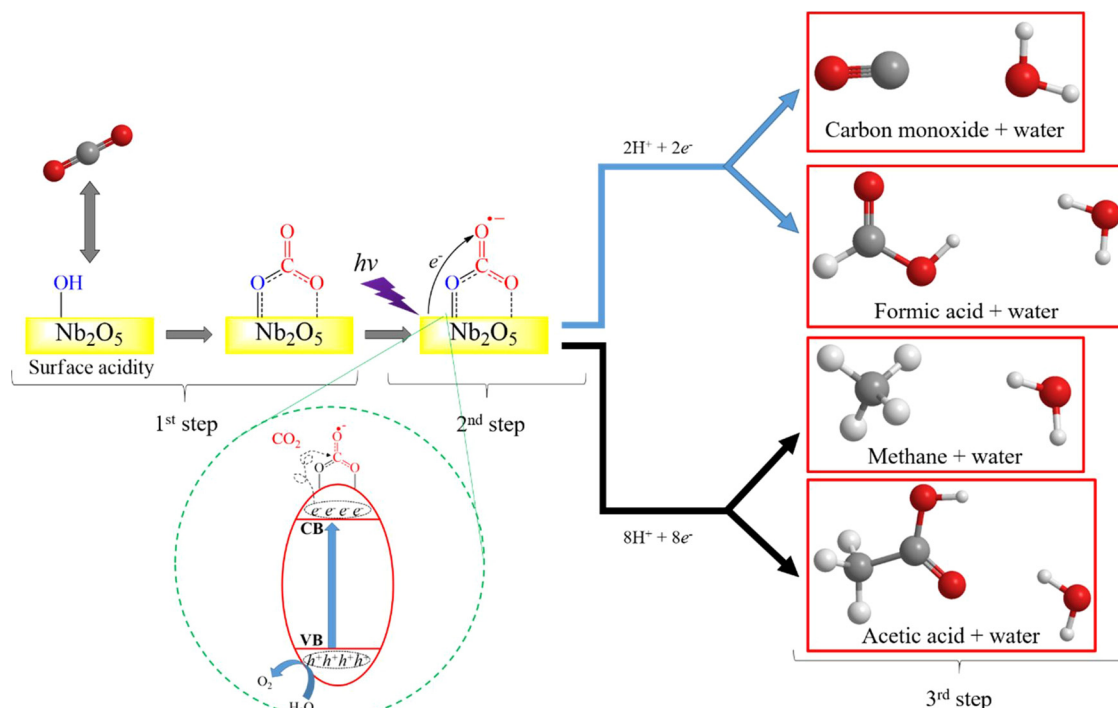
The other products such as methane (CH<sub>4</sub>) and acetic acid (CH<sub>3</sub>COOH) are more difficult to be formed in this system, once this requires eight electrons and eight protons as well as the adsorption of CO on the catalyst surface or the CO dissolution in the aqueous medium (3<sup>rd</sup> step) [59,61–63]. The high CH<sub>3</sub>COOH yields obtained from catalysts with the highest surface acidity may be associated with the fact that the reactor headspace saturation increases the CO partial pressure and its solubility in the aqueous medium [46,47]. Catalysts with poorly hydroxylated surfaces seem to be more active for CO adsorption, which could explain the increased CH<sub>4</sub> production observed for Nb-400 °C.

#### 4. Conclusion

We have shown for the first time that Nb<sub>2</sub>O<sub>5</sub> is an active catalyst for CO<sub>2</sub> photoreduction in which the Nb<sub>2</sub>O<sub>5</sub> surface acidity plays a significant role in its selectivity towards byproducts. This effect is probably related to the formation of intermediates due to the CO<sub>2</sub> adsorbed onto the Nb<sub>2</sub>O<sub>5</sub> surface by coordination of oxygen atoms and further reaction with H<sup>+</sup>. The CO<sub>2</sub> photoreduction efficiency was surface acidity-dependent: high surface acidity prompted conversion of CO<sub>2</sub> preferentially to CO, HCOOH, and CH<sub>3</sub>COOH, while low surface acidity prompted CO<sub>2</sub> conversion preferentially towards CH<sub>4</sub>. It was demonstrated that CO is the main intermediate species of the CO<sub>2</sub> photoreduction in all conditions. The high activity of the acid Nb<sub>2</sub>O<sub>5</sub> catalysts in comparison with other systems reported in the literature indicates that the photocatalytic properties of Nb<sub>2</sub>O<sub>5</sub> deserve further investigation for CO<sub>2</sub> reduction.

#### Acknowledgments

The authors are grateful to the Ministry of Science, Technology, and Innovation (SisNANO Program – National System of Laboratories in Nanotechnology), the National Council for Scientific and Technological



Scheme 1. Proposed pathways for CO<sub>2</sub> photoreduction adsorbed on the acid surface of Nb<sub>2</sub>O<sub>5</sub>.



Development (CNPq, Brazil China Virtual Center in Nanotechnology Project and grant #402.287/2013-4), Coordination for the Improvement of Higher Education Personnel (CAPES) (Finance code 001), Sao Paulo Research Foundation (FAPESP grants #15/14330-8, #16/21515-7, #16/09746-3), and Embrapa Rede AgroNano for their financial support. Caue Ribeiro also acknowledges Chinese Academy of Sciences (CAS) President's International Fellowship Initiative (PIFI) by the financial support. We thank the Brazilian Nanotechnology Laboratory for Research in Energy and Materials (LNNano) and the Structural Characterization Laboratory (LCE) for technical support in the X-ray photoelectron spectroscopy (grant #13839) and transmission electron microscopy experiments, respectively.

## Appendix A. Supplementary data

Supplementary material related to this article can be found, in the online version, at doi:<https://doi.org/10.1016/j.apcatb.2018.10.017>.

## References

- [1] C. Huntingford, L.M. Mercado, High chance that current atmospheric greenhouse concentrations commit to warmings greater than 1.5°C over land, *Nat. Publ. Gr.* (2016) 1–7.
- [2] A. Stips, D. Macias, C. Coughlan, E. Garcia-gorrix, X.S. Liang, On the causal structure between CO<sub>2</sub> and global temperature, *Sci. Rep.* (2016) 1–9.
- [3] WMO, The state of greenhouse gases in the atmosphere based on global observations through 2016, *Greenh. Gas Bull.* (2017) 1–4.
- [4] K. Li, X. An, K.H. Park, M. Khraish, J. Tang, A critical review of CO<sub>2</sub> photocatalytic conversion: catalysts and reactors, *Catal. Today* 224 (2014) 3–12, <https://doi.org/10.1016/j.cattod.2013.12.006>.
- [5] S. Bai, W. Yin, L. Wang, Z. Li, Y. Xiong, Surface and interface design in cocatalysts for photocatalytic water splitting and CO<sub>2</sub> reduction, *RSC Adv.* 6 (2016) 57446–57463, <https://doi.org/10.1039/C6RA10539D>.
- [6] Y. He, Y. Wang, L. Zhang, B. Teng, M. Fan, High-efficiency conversion of CO<sub>2</sub> to fuel over ZnO/g-C<sub>3</sub>N<sub>4</sub> photocatalyst, *Appl. Catal. B Environ.* 168 (2015) 1–8.
- [7] S.N. Habisreutinger, L. Schmidt-Mende, J.K. Stolarczyk, Photocatalytic reduction of CO<sub>2</sub> on TiO<sub>2</sub> and other semiconductors, *Angew. Chem. Int. Ed.* 52 (2013) 7372–7408, <https://doi.org/10.1002/anie.201207199>.
- [8] Z. Li, J. Feng, S. Yan, Z. Zou, Solar fuel production: strategies and new opportunities with nanostructures, *Nano Today* (2015) 1–19.
- [9] L. Yuan, Y.-J. Xu, Photocatalytic conversion of CO<sub>2</sub> into value-added and renewable fuels, *Appl. Surf. Sci.* 342 (2015) 154–167, <https://doi.org/10.1016/j.apsusc.2015.03.050>.
- [10] X. Liu, S. Inagaki, J. Gong, Heterogeneous molecular systems for photocatalytic CO<sub>2</sub> reduction with water oxidation, *Angew. Chem. Int. Ed.* 55 (2016) 14924–14950, <https://doi.org/10.1002/anie.201600395>.
- [11] J.A. Oliveira, A.E. Nogueira, M.C.P. Gonc, E.C. Paris, C. Ribeiro, G.Y. Poirier, T.R. Giraldo, Applied surface science photoactivity of N-doped ZnO nanoparticles in oxidative and reductive reactions, *Appl. Surf. Sci.* 433 (2018) 879–886, <https://doi.org/10.1016/j.apsusc.2017.10.110>.
- [12] J. Kou, C. Lu, J. Wang, Y. Chen, Z. Xu, R.S. Varma, Selectivity enhancement in heterogeneous photocatalytic transformations, *Chem. Rev.* 117 (2017) 1445–1514, <https://doi.org/10.1021/acs.chemrev.6b00396>.
- [13] I.H. Tseng, W.C. Chang, J.C.S. Wu, Photoreduction of CO<sub>2</sub> using sol-gel derived titania and titania-supported copper catalysts, *Appl. Catal. B Environ.* 37 (2002) 37–48, [https://doi.org/10.1016/S0926-3373\(01\)00322-8](https://doi.org/10.1016/S0926-3373(01)00322-8).
- [14] Q. Li, L. Zong, C. Li, J. Yang, Photocatalytic reduction of CO<sub>2</sub> on MgO/TiO<sub>2</sub> nanotube films, *Appl. Surf. Sci.* 314 (2014) 458–463, <https://doi.org/10.1016/j.apsusc.2014.07.019>.
- [15] F. Sastre, A. Corma, H. García, 185 nm photoreduction of CO<sub>2</sub> to methane by water. Influence of the presence of a basic catalyst, *J. Am. Chem. Soc.* 134 (2012) 14137–14141, <https://doi.org/10.1021/ja304930t>.
- [16] K. Bhattacharyya, A. Danon, B.K. Vijayan, K.A. Gray, P.C. Stair, E. Weitz, Role of the surface lewis acid and base sites in the adsorption of CO<sub>2</sub> on titania nanotubes and platinumized titania nanotubes: an in situ FT-IR study, *J. Phys. Chem. C* 117 (2013) 12661–12678.
- [17] S. Civiš, M. Ferus, A. Křižek, P. Kubelík, L. Kavan, M. Zúkalová, Photocatalytic transformation of CO<sub>2</sub> to CH<sub>4</sub> and CO on acidic surface of TiO<sub>2</sub>anatase, *Opt. Mater. (Amst.)* 56 (2016) 80–83, <https://doi.org/10.1016/j.optmat.2015.11.015>.
- [18] J. Jiao, Y. Wei, Y. Zhao, Z. Zhao, A. Duan, J. Liu, Y. Pang, J. Li, G. Jiang, Y. Wang, AuPd/3DOM-TiO<sub>2</sub> catalysts for photocatalytic reduction of CO<sub>2</sub>: High efficient separation of photogenerated charge carriers, *Appl. Catal. B Environ.* 209 (2017) 228–239, <https://doi.org/10.1016/j.apcatb.2017.02.076>.
- [19] M. Luisa Marin, G.L. Hallett-Tapley, S. Impellizzeri, C. Fasciani, S. Simoncelli, J.C. Netto-Ferreira, J.C. Scaiano, Synthesis, acid properties and catalysis by niobium oxide nanostructured materials, *Catal. Sci. Technol.* 4 (2014) 3044–3052, <https://doi.org/10.1039/C4CY00238E>.
- [20] K. Nakajima, Y. Baba, R. Noma, M. Kitano, J.N. Kondo, S. Hayashi, M. Hara, Nb<sub>2</sub>O<sub>5</sub>·nH<sub>2</sub>O as a heterogeneous catalyst with water-Tolerant Lewis acid sites, *J. Am. Chem. Soc.* 133 (2011) 4224–4227, <https://doi.org/10.1016/j.jleao.2015.05.036>.
- [21] O.F. Lopes, V.R. De Mendonça, F.B.F. Silva, E.C. Paris, C. Ribeiro, Niobium oxides: an overview of the synthesis of Nb<sub>2</sub>O<sub>5</sub> and its application in heterogeneous photocatalysis, *Quim. Nova* 38 (2014) 106–117, <https://doi.org/10.5935/0100-4042.20140280>.
- [22] A. Esteves, L.C.A. Oliveira, T.C. Ramalho, M. Goncalves, A.S. Anastacio, H.W.P. Carvalho, New materials based on modified synthetic Nb<sub>2</sub>O<sub>5</sub> as photocatalyst for oxidation of organic contaminants, *Catal. Commun.* 10 (2008) 330–332, <https://doi.org/10.1016/j.jcatcom.2008.09.012>.
- [23] O.F. Lopes, E.C. Paris, C. Ribeiro, Synthesis of Nb<sub>2</sub>O<sub>5</sub> nanoparticles through the oxidant peroxide method applied to organic pollutant photodegradation: a mechanistic study, *Appl. Catal. B Environ.* 144 (2014) 800–808.
- [24] H. Liu, N. Gao, M. Liao, X. Fang, Hexagonal-like Nb<sub>2</sub>O<sub>5</sub> nanoplates-based photo-detectors and photocatalyst with high performances, *Sci. Rep.* 5 (2015) 7716, <https://doi.org/10.1038/srep07716>.
- [25] G.T.S.T. da Silva, K.T.G. Carvalho, O.F. Lopes, C. Ribeiro, g-C<sub>3</sub>N<sub>4</sub>/Nb<sub>2</sub>O<sub>5</sub> heterostructures tailored by sonochemical synthesis: enhanced photocatalytic performance in oxidation of emerging pollutants driven by visible radiation, *Appl. Catal. B Environ.* 216 (2017) 70–79, <https://doi.org/10.1016/j.apcatb.2017.05.038>.
- [26] K.T.G. Carvalho, A.E. Nogueira, O.F. Lopes, G. Byzinski, C. Ribeiro, Synthesis of g-C<sub>3</sub>N<sub>4</sub>/Nb<sub>2</sub>O<sub>5</sub> heterostructures and their application on removal of organic pollutants under visible and ultraviolet irradiation, *Ceram. Int.* 43 (2016) 3521–3530, <https://doi.org/10.1016/j.ceramint.2016.11.063>.
- [27] E.V. Savinkina, L.N. Obolenskaya, G.M. Kuzmicheva, I.D. Morozov, R.G. Chumakov, Effects of peroxo precursors and annealing temperature on properties and photocatalytic activity of nanoscale titania, *J. Mater. Res.* 33 (2018) 1422–1432, <https://doi.org/10.1557/jmr.2018.52>.
- [28] L. Forni, Comparison of the methods for the determination of surface acidity of solid catalysts, *Catal. Rev. Sci. Eng.* 8 (2012) 65–115 1974.
- [29] K.M.A. Santos, E.M. Albuquerque, L.E.P. Borges, M.A. Fraga, Discussing Lewis and Brønsted acidity on continuous pyruvaldehyde Cannizzaro reaction to lactic acid over solid catalysts, *Mol. Catal.* 458 (2017) 198–205, <https://doi.org/10.1016/j.mcat.2017.12.010>.
- [30] Y. Zhao, X. Zhou, L. Ye, S.C.E. Tsang, Nanostructured Nb<sub>2</sub>O<sub>5</sub> catalysts, *Nano Rev.* 3 (2012) 1–11, <https://doi.org/10.3402/nr.v3i0.17631>.
- [31] C. Guo, Z. Qian, Acidic and catalytic properties of niobic acid crystals low temperature, *Catal. Today* 16 (1993) 379–385, [https://doi.org/10.1016/0920-5861\(93\)80077-E](https://doi.org/10.1016/0920-5861(93)80077-E).
- [32] S. Li, Q. Xu, E. Uchaker, X. Cao, G. Cao, Comparison of amorphous, pseudohexagonal and orthorhombic Nb<sub>2</sub>O<sub>5</sub> for high-rate lithium ion insertion, *CrystEngComm* 18 (2016) 2532–2540, <https://doi.org/10.1039/c5ce02069g>.
- [33] J. Xue, R. Wang, Z. Zhang, S. Qiu, Facile preparation of C, N co-modified Nb<sub>2</sub>O<sub>5</sub> nanoneedles with enhanced visible light photocatalytic activity, *Dalton Trans.* 45 (2016) 16519–16525, <https://doi.org/10.1039/C6DT03548E>.
- [34] M. Ristic, S. Popovic, S. Music, Sol-gel synthesis and characterization of Nb<sub>2</sub>O<sub>5</sub> powders, *Mater. Lett.* 58 (2004) 2658–2663, <https://doi.org/10.1016/j.matlet.2004.03.041>.
- [35] E.R. Leite, C. Vila, J. Bettini, E. Longo, Synthesis of Niobia Nanocrystals with Controlled Morphology, (2006), pp. 18088–18090.
- [36] C. Paragassú Cecchi, D. Cesarín-Sobrinho, A. Buarque Ferreira, J. Netto-Ferreira, New insights on the oxidation of unsaturated fatty acid methyl esters catalyzed by niobium(V) oxide. A study of the catalyst surface reactivity, *Catalysts* 8 (2018) 6, <https://doi.org/10.3390/catal8010006>.
- [37] R.F. Brandão, R.L. Quirino, V.M. Mello, A.P. Tavares, A.C. Peres, F. Guinhos, J.C. Rubim, P.A.Z. Suarez, Synthesis, characterization and use of Nb<sub>2</sub>O<sub>5</sub> based catalysts in producing biofuels by transesterification, esterification and pyrolysis, *J. Braz. Chem. Soc.* 20 (2009) 954–966, <https://doi.org/10.1590/S0103-50532009000500022>.
- [38] Y. Hong, C. Li, G. Zhang, Y. Meng, B. Yin, Y. Zhao, W. Shi, Efficient and stable Nb<sub>2</sub>O<sub>5</sub> modified g-C<sub>3</sub>N<sub>4</sub> photocatalyst for removal of antibiotic pollutant, *Chem. Eng. J.* 299 (2016) 74–84, <https://doi.org/10.1016/j.cej.2016.04.092>.
- [39] X. Ma, Y. Chen, H. Li, X. Cui, Y. Lin, Annealing-free synthesis of carbonaceous Nb<sub>2</sub>O<sub>5</sub> microspheres by flame thermal method and enhanced photocatalytic activity for hydrogen evolution, *Mater. Res. Bull.* 66 (2015) 51–58, <https://doi.org/10.1016/j.materresbull.2015.02.005>.
- [40] S. Ge, H. Jia, H. Zhao, Z. Zheng, L. Zhang, First observation of visible light photocatalytic activity of carbon modified Nb<sub>2</sub>O<sub>5</sub> nanostructures, *J. Mater. Chem.* 20 (2010) 3052, <https://doi.org/10.1039/b923586h>.
- [41] M.E. Aguirre, R. Zhou, A.J. Eugene, M.I. Guzman, M.A. Grela, Cu<sub>2</sub>O/TiO<sub>2</sub> heterostructures for CO<sub>2</sub> reduction through a direct Z-scheme: protecting Cu<sub>2</sub>O from photocorrosion, *Appl. Catal. B Environ.* 217 (2017) 485–493, <https://doi.org/10.1016/j.apcatb.2017.05.058>.
- [42] X. Chang, T. Wang, J. Gong, CO<sub>2</sub> photoreduction: insights into CO<sub>2</sub> activation and reaction on surfaces of photocatalysts, *Energy Environ. Sci.* 9 (2016) 2177–2196, <https://doi.org/10.1039/C6EE00383D>.
- [43] T. Yui, A. Kan, C. Saitoh, K. Koike, O. Ishitani, Photochemical reduction of CO<sub>2</sub> using TiO<sub>2</sub>: effects of organic adsorbates on TiO<sub>2</sub> and deposition of Pd onto TiO<sub>2</sub>, *ACS Appl. Mater. Interfaces* 3 (2011) 2594–2600, <https://doi.org/10.1021/am200425y>.
- [44] E.L.P.J.V. Hillman, Carbon monoxide, in: R.D.H.M.B.T. Johnson (Ed.), *Hamilt. Hardy's Ind. Toxicol.* 6th ed., WILEY, 2015, pp. 309–316.
- [45] J.A. Dean, McGRAW-HILL, INC, *Lange's Handbook of Chemistry*, 15th ed., (1999).
- [46] R. Sander, Compilation of Henry's law constants (version 4.0) for water as solvent, *Atmos. Chem. Phys.* 15 (2015) 4399–4981, <https://doi.org/10.5194/acp-15-4399-2015>.
- [47] IUPAC, *Compendium of Chemical Terminology*, 2nd ed., Blackwell Scientific



- Publications, Oxford, 1997.
- [48] E. Karamian, S. Sharifnia, On the general mechanism of photocatalytic reduction of CO<sub>2</sub>, *J. CO<sub>2</sub> Util.* 16 (2016) 194–203, <https://doi.org/10.1016/j.jcou.2016.07.004>.
- [49] J.-P. Jones, G.K.S. Prakash, G.A. Olah, Electrochemical CO<sub>2</sub> reduction: recent advances and current trends, *Isr. J. Chem.* 54 (2014) 1451–1466, <https://doi.org/10.1002/ijch.201400081>.
- [50] S.R. Lingampalli, M.M. Ayyub, C.N.R. Rao, Recent progress in the photocatalytic reduction of carbon dioxide, *ACS Omega* 2 (2017) 2740–2748, <https://doi.org/10.1021/acsomega.7b00721>.
- [51] J. Alboa, M. Alvarez-Guerra, P. Castaño, A. Irabien, Towards the electrochemical conversion of carbon dioxide into methanol, *Green Chem.* 17 (2015) 2304–2324, <https://doi.org/10.1039/C4GC02453B>.
- [52] X. Chang, T. Wang, J. Gong, CO<sub>2</sub> photo-reduction: insights into CO<sub>2</sub> activation and reaction on surfaces of photocatalysts, *Energy Environ. Sci.* 9 (2016) 2177–2196, <https://doi.org/10.1039/c6ee00383d>.
- [53] D. Ren, J. Fong, B.S. Yeo, The effects of currents and potentials on the selectivities of copper toward carbon dioxide electroreduction, *Nat. Commun.* 9 (2018), <https://doi.org/10.1038/s41467-018-03286-w>.
- [54] R. Kortlever, J. Shen, K.J.P. Schouten, F. Calle-Vallejo, M.T.M. Koper, Catalysts and reaction pathways for the electrochemical reduction of carbon dioxide, *J. Phys. Chem. Lett.* 6 (2015) 4073–4082, <https://doi.org/10.1021/acs.jpclett.5b01559>.
- [55] C. Sci, K.J.P. Schouten, Y. Kwon, C.J.M. Van Der Ham, Z. Qin, M.T.M. Koper, A new mechanism for the selectivity to C 1 and C 2 species in the electrochemical reduction of carbon dioxide on copper electrodes, *Chem. Sci.* 2 (2011) 1902–1909, <https://doi.org/10.1039/c1sc00277e>.
- [56] C. Deleitenburg, A. Trovarelli, Metal-support interactions in Rh/CeO<sub>2</sub>, Rh/TiO<sub>2</sub>, and Rh/Nb<sub>2</sub>O<sub>5</sub> catalysts as inferred from CO<sub>2</sub> methanation activity, *J. Catal.* 156 (1995) 174–174.
- [57] Y. Zhao, Y. Wei, X. Wu, H. Zheng, Z. Zhao, J. Liu, J. Li, Graphene-wrapped Pt/TiO<sub>2</sub> photocatalysts with enhanced photogenerated charges separation and reactant adsorption for high selective photoreduction of CO<sub>2</sub> to CH<sub>4</sub>, *Appl. Catal. B Environ.* 226 (2018) 360–372, <https://doi.org/10.1016/j.apcatb.2017.12.071>.
- [58] Y. Wei, X. Wu, Y. Zhao, L. Wang, Z. Zhao, X. Huang, J. Liu, J. Li, Efficient photocatalysts of TiO<sub>2</sub> nanocrystals-supported PtRu alloy nanoparticles for CO<sub>2</sub> reduction with H<sub>2</sub>O: synergistic effect of Pt-Ru, *Appl. Catal. B Environ.* 236 (2018) 445–457, <https://doi.org/10.1016/j.apcatb.2018.05.043>.
- [59] S.S. Meryem, S. Nasreen, M. Siddique, R. Khan, An overview of the reaction conditions for an efficient photoconversion of CO<sub>2</sub>, *Rev. Chem. Eng.* 37 (2017) 409–425, <https://doi.org/10.1515/revce-2016-0016>.
- [60] W.N. Wang, J. Souli, Y. Jeffrey Yang, P. Biswas, Comparison of CO<sub>2</sub> photoreduction systems: a review, *Aerosol Air Qual. Res.* 14 (2014) 533–549, <https://doi.org/10.4209/aaqr.203.09.0283>.
- [61] Q. Guo, Q. Zhang, H. Wang, Z. Liu, Z. Zhao, Unraveling the role of surface property in the photoreduction performance of CO<sub>2</sub> and H<sub>2</sub> O catalyzed by the modified ZnO, *Mol. Catal.* 436 (2017) 19–28, <https://doi.org/10.1016/j.mcat.2017.04.014>.
- [62] C. Genovese, C. Ampelli, S. Perathoner, G. Centi, Mechanism of C-C bond formation in the electrocatalytic reduction of CO<sub>2</sub> to acetic acid. A challenging reaction to use renewable energy with chemistry, *Green Chem.* (2017) 2406–2415, <https://doi.org/10.1039/c6gc03422e>.
- [63] X. Sun, Q. Zhu, X. Kang, H. Liu, Q. Qian, J. Ma, Z. Zhang, G. Yang, B. Han, Design of a Cu(I)/C-doped boron nitride electrocatalyst for efficient conversion of CO<sub>2</sub> into acetic acid, *Green Chem.* (2017) 2086–2091, <https://doi.org/10.1039/c7gc00503b>.